

Molecular orientation in soft matter thin films studied by resonant soft x-ray reflectivityMarkus Mezger,^{1,2,*} Blandine Jérôme,² Jeffrey B. Kortright,² Manuel Valdiviares,^{2,†} Eric M. Gullikson,² Angelo Giglia,³ Nicola Mahne,³ and Stefano Nannarone^{3,4}¹*Department of Chemical Engineering, University of California, Berkeley, California 94720, USA*²*Materials Sciences Division, Lawrence Berkeley National Laboratory, Berkeley, California 94720, USA*³*Istituto Officina dei Materiali del Consiglio Nazionale delle Ricerche, I-34149 Trieste, Italy*⁴*Dipartimento di Ingegneria dei Materiali e dell'Ambiente, Università di Modena and Reggio Emilia, I-41100 Modena, Italy*

(Received 12 January 2011; published 5 April 2011)

We present a technique to study depth profiles of molecular orientation in soft matter thin films with nanometer resolution. The method is based on dichroism in resonant soft x-ray reflectivity using linear *s* and *p* polarization. It combines the chemical sensitivity of near-edge x-ray absorption fine structure spectroscopy to specific molecular bonds and their orientation relative to the polarization of the incident beam with the precise depth profiling capability of x-ray reflectivity. We demonstrate these capabilities on side chain liquid crystalline polymer thin films with soft x-ray reflectivity data at the carbon *K* edge. Optical constants of the anisotropic refractive index ellipsoid were obtained from a quantitative analysis using the Berreman formalism. For films up to 50 nm thickness we find that the degree of orientation of the long axis exhibits no depth variation and is independent of the film thickness.

DOI: [10.1103/PhysRevB.83.155406](https://doi.org/10.1103/PhysRevB.83.155406)

PACS number(s): 61.05.cm, 61.05.cj, 61.30.Vx, 68.55.am

I. INTRODUCTION

X-ray reflectivity (XRR) offers a powerful tool to study a wide class of surfaces and buried interfaces with molecular scale resolution.^{1,2} By modulating the contrast, resonant or anomalous x-ray scattering techniques exploit the characteristic absorption spectra of atoms and molecular states to access element- and bond-specific information beyond the pure electron density distributions.^{3,4} Near-edge x-ray absorption fine structure (NEXAFS) spectroscopy⁵ employs the absorption dichroism for x rays polarized parallel (*p*) and perpendicular (*s*) to the incidence plane, to obtain the orientation of specific molecular bonds. At a given x-ray resonance, absorption depends on the direction of the electric-field vector of the incident x-ray beam with respect to the associated molecular orbital. The optical theorem links this anisotropy to the imaginary part of the refractive index from which its real part can be obtained by Kramers-Kronig transformation. Thus, it should in principle be possible to obtain depth profiles of molecular orientation in a stratified system with nm resolution from resonant XRR measurements in *s* and *p* incidence.

In contrast to established NEXAFS spectroscopy techniques with their specific probing depths of approximately 1 nm for partial electron yield, up to 10 nm for total electron yield (TEY), and hundreds of nanometers for fluorescence yield, resonant soft x-ray reflectivity (XRR) data carry full depth-dependent information with nanometer resolution through structures up to several hundred nm thickness ranging from buried interfaces to the free surface.^{6,7} It is this unique depth profiling capability on the molecular length scale that distinguishes it from other established experimental methods such as nonlinear optical techniques. Analogous resonant x-ray reflectivity techniques that employ the contrast of magnetic circular dichroism are successfully used to study magnetization profiles in thin films.^{8,9} Stoichiometry changes and distortions in the near-surface region of strontium titanate were found by self-consistent modeling of x-ray reflectivity data in *s* and *p* incidence.¹⁰ However, except for one ellipsometry-type

experiment on highly oriented pyrolytic graphite¹¹ and its suggestion by different authors,^{1,12} polarization-dependent resonant XRR experiments at the carbon *K* edge on organic soft matter thin films have not been reported. While this idea of depth profiling the orientation of anisotropic molecular entities is of obvious interest and relevance to many systems, the proper optical description of systems having overlapping spectral features each with potentially different polarization dependence is nontrivial and needs to be demonstrated.

Here we present a study where molecular orientation in a polymer thin film is obtained from polarization-dependent resonant XRR experiments. We show that reflectivity curves recorded in *s* and *p* incidence across soft x-ray absorption resonances of oriented functional groups at the carbon *K* edge exhibit strong linear dichroism that can be quantitatively analyzed using the Berreman matrix formalism for reflection and transmission in anisotropic stratified systems.¹³ To demonstrate this novel capability, we have studied the side-chain orientation of liquid crystalline polymer (LCP) thin films. Poly(2-4-[(4-cyanophenoxy) carbonyl]phenoxyethyl acrylate) (structure in Fig. 1) has a glass transition temperature of 75 °C and forms a nematic liquid crystalline phase below 111 °C.^{14,15} These films are excellent model systems to demonstrate the sensitivity of XRR to molecular orientation, as the stiff elongated side groups tend to align parallel to each other even in bulk and take specific orientations close to interfaces.¹⁶ Optical dichroic measurements at the free surface showed an in-plane alignment of the optical axis.¹⁷

II. MATERIALS AND METHODS**A. LCP thin film samples**

Thin poly(2-4-[(4-cyanophenoxy) carbonyl]phenoxy)ethyl acrylate (Merck, Darmstadt; LCP100) films were prepared on silicon wafers [Siltronics, Munich; (100) orientation, *p*-type boron-doped, 10–20 Ω cm resistance, 625 μm thickness] covered with a native oxide layer. The

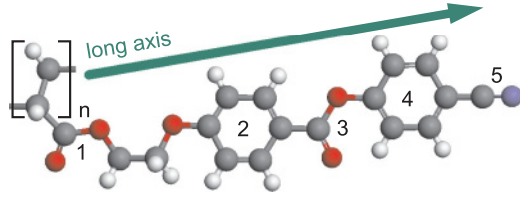


FIG. 1. (Color online) Sketch of the side chain liquid crystalline polymer poly(2-4-[(4-cyanophenoxy) carbonyl]phenoxyethyl acrylate) containing two ester (COO, 1 and 3), two phenylene (C_6H_4 , 2 and 4), and one nitrile group (CN, 5) per monomer. The arrow indicates the long axis of the side chain. In the nematic liquid crystalline phase, the optical axis of the material is defined by the average direction of the long axis of all side chains.

wafers were cut in pieces of 0.5 in. \times 0.5 in. and solvent cleaned (acetone, isopropanol) in an ultrasonic bath. To remove organic contaminations, the substrates were immersed in a freshly prepared piranha solution (one part H_2O_2 35% and three parts H_2SO_4 98%) overnight. (Warning: Piranha solution should be handled with extreme care; in some circumstances, particularly when contacted with significant quantities of an oxidizable organic material, it can detonate spontaneously.) After thorough rinsing with ultrapure water (Millipore Gradient; 18.2M Ω cm) the hydrophilic substrates were kept under water in a sealed container for further use. LCP solutions in nitromethane (Acros; 99% p.a.) were prepared in a concentration of 0.26 and 1.00 wt.%. The substrates were spun dried in a laminar flow cabinet. Homogeneous thin LCP films of variable thicknesses between 8 and 50 nm and a rms surface roughness below 1 nm were prepared by spin coating the LCP solutions between 750 and 3000 rpm (acceleration 4000 rpm/s, see Table I) after filtering through 0.4 μ m Teflon syringe filters. The equilibrium nematic structure was reached by thermal annealing under vacuum.

B. NEXAFS spectroscopy

Total electron yield NEXAFS spectra were recorded at BL6.3.2 (Refs. 18 and 19) at the Advanced Light Source (ALS) for *s* and *p* polarization at a grazing angle of 20° and

TABLE I. Summary of LCP thin film sample preparation (LCP solution concentration, spinning speed, annealing) and characterization parameters (LCP film thickness t , mass density ρ , surface roughness σ) obtained by fitting of off-resonant (250 eV) XRR data.¹⁵ Beamline (BL) details are provided in the Appendix.

No.	Conc. (wt. %)	Speed (rpm)	Annealing	t (nm)	ρ (g/cm ³)	σ (nm)	BL
A	0.26	3000	18.5h@95 °C	7.1	1.25	0.6	1
A'				7.4	1.17	0.5	3
B	0.26	1500	38.0h@100 °C	9.6	1.24	0.7	1
B'				9.8	1.15	0.5	3
C	0.62	750	18.5h@95 °C	28.6	1.16	0.4	2
C'				29.5	1.17	0.5	3
D ₁	1.00	750	38.0h@100 °C	49.0	1.26	0.8	1
D ₁ '				50.8	1.20	0.6	3
D ₂	1.00	750	38.0h@100 °C	47.6	1.14	0.5	2
D ₂ '				94.3	1.19	0.6	3

at normal incidence. The energy resolution around the carbon *K* edge (284 eV) was set to 0.1 eV. Higher harmonics were suppressed by a 0.6 μ m titanium filter. An external voltage of 9 V was applied between the vacuum chamber and the sample and the biased sample drain photo-current was measured with a pico-amperemeter. Data were taken in *s* and *p* polarization at a grazing angle of 20° and at normal incidence on two different samples with an LCP film thickness of approximately 30 nm. Subsequent measurements at the same spot and at different sample positions confirmed that no significant beam damage occurred during data collection. The raw data were normalized by the synchrotron ring current and corrected for the beamline spectrum measured separately with a silicon photodiode. After background correction, the data were scaled to the x-ray absorption coefficients μ taken from the CXRO database²⁰ and corrected for saturation effects at the low incidence angles⁵ by

$$\mu = \frac{\mu' \sin \theta}{\sin \theta - \mu' L} \quad (1)$$

with an effective electron escape depth $L = 6$ nm determined from the angle-dependent TEY signal in *s* polarization.

C. Resonant x-ray reflectivity

Figure 2 shows a sketch of the scattering geometry for the polarization-dependent XRR measurements.

The experiments in *s* and *p* polarization were performed in a mobile UHV scattering chamber at an Apple-II Elliptically Polarizing Undulator at BL4.0.2 at the ALS and at the BEAR end station at ELETTRA (see the Appendix for beamline details). A set of silver absorbers (Lebow, thickness 0.6, 1.0, or 1.5 μ m) adjusted the flux and filtered higher harmonic contaminations and stray light from the monochromator in the incident beam spectrum. The reflected intensity spanning a dynamic range of more than six orders of magnitude was detected with a channel electron multiplier (Sjuts, Extended Dynamic Range CEM). Outperforming commonly used diode detectors, their high sensitivity and low dark count rate allow fast XRR measurements with low x-ray dose to avoid beam damage on the sample. XRR patterns $R_{s/p}(E, \theta)$ were recorded in *s* and *p* polarization as energy scans at a constant grazing angle and for fixed x-ray energies between 284.4 and 288.0 eV, i.e., around the carbon *K* edge, by $\theta/2\theta$ scans from grazing incidence up to a maximum vertical momentum transfer of $q = 2.2$ nm⁻¹. Dead time of the detector and counting electronics was corrected by a generic factor $(1 - N\tau)^{-1}$ with the count rate N and an instrument-specific time constant τ determined from reflectivity measurements of a silicon sample with different filter settings. The background of the

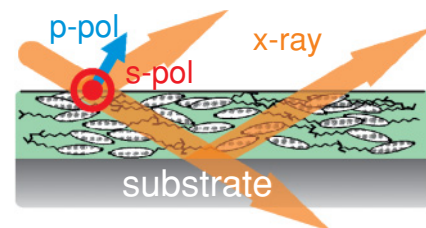


FIG. 2. (Color online) Sketch of the setup for the polarization-dependent XRR experiments.

TABLE II. Vertical d_v and horizontal d_h beam size (FWHM) and effective footprint on the sample l for an incident angle θ of 10° , 20° , and 40° at beamline BL4.0.2 (1), BEAR (2), and BL6.3.2 (3).

BL	d_v (μm)	d_h (μm)	l_{10° (μm)	l_{20° (μm)	l_{40° (μm)
1	100	100	580	290	160
2 <i>s</i> pol	40	150	230	120	NA
2 <i>p</i> pol	150	40	860	440	NA
3	30	300	170	90	50

reflectivity data measured with a CEM was only significant in *p* incidence around the Brewster angle, and a constant background of 10^{-6} was subtracted from the experimental data. A correction of the beam footprint $l_\theta = d_v / \sin \theta$ on the sample of length $l_s = 1.3$ mm at grazing angles θ was applied by $\text{erf}(0.83 l_s / l_\theta)$ assuming a vertical Gaussian intensity distribution in the primary beam [full width at half maximum (FWHM); see Table II]. Reflectivity data versus energy were normalized by the incident photon flux measured separately with a silicon photodiode. Off-resonant reflectivity curves at 250 eV ensured that the observed resonant $R(q)$ anisotropy is not caused by misalignment or instrumental artifacts, and rather originates from the orientational order of the LCP thin films. Additional XRR data in *s* polarization for sample characterization and cross checks were collected at BL6.3.2 at the ALS.

III. RESULTS AND DISCUSSIONS

A. Spectroscopy and refractive index

Figure 3(a) shows normalized NEXAFS TEY spectra for *s* and *p* incidence at $\theta = 20^\circ$. Resonances at 285.2, 286.6, and 288.6 eV are associated with the π^* transitions from the *K* shell to the empty antibinding molecular orbitals of the phenylene, nitrile, and ester groups (see Fig. 1), respectively.²¹ Pronounced dichroism indicates an anisotropic orientation of the LCP side chains in the near-surface region. Increased absorption at the phenylene and nitrile π^* resonances in *p* incidence is consistent with a structure where the side chains lay preferentially parallel to the surface. The absence of strong dichroism above 287 eV is consistent with larger orientational freedom of the C=O bond in the ester group.

Refractive index $n(E) = 1 - \delta + i\beta$ and x-ray form factors $f(E) = f_1 + if_2$ are linked to the absorption coefficient μ by the optical theorem, while δ and β are connected through the Kramers-Kronig transformation^{20,22} via

$$f_1 = Z^* + \frac{2}{\pi} \int_0^\infty d\epsilon \frac{\epsilon}{E^2 - \epsilon^2} f_2, \quad (2a)$$

$$= \frac{2\pi}{\lambda^2 \rho_M N_A r_e} \delta, \quad (2b)$$

$$f_2 = \frac{\mu}{\lambda \rho_M N_A r_e}, \quad (2c)$$

$$= \frac{2\pi}{\lambda^2 \rho_M N_A r_e} \beta, \quad (2d)$$

where Z^* denotes the relativistic corrected number of electrons.²³ The Kramers-Kronig transformation was calcu-

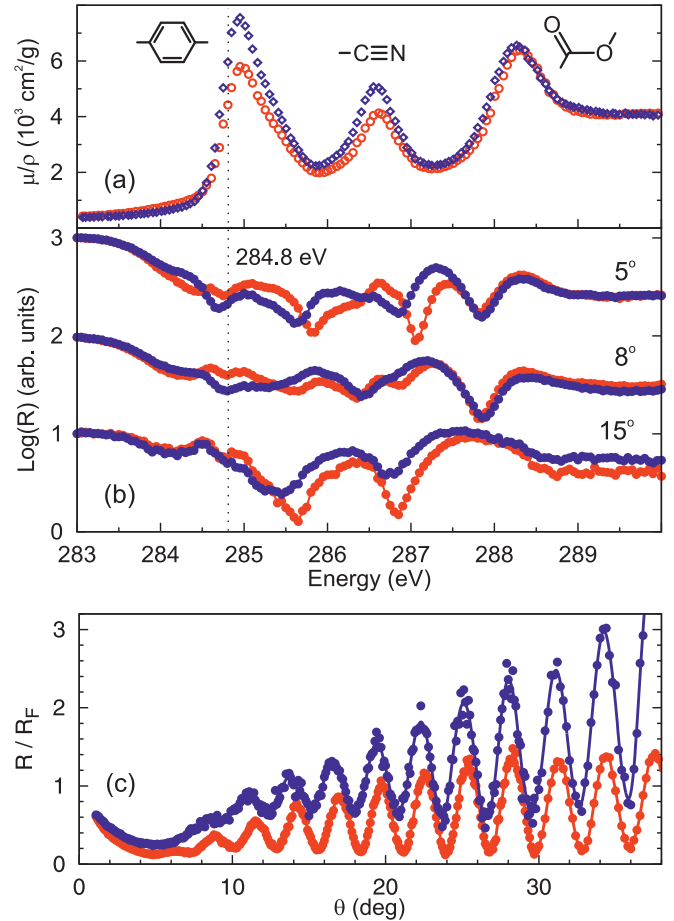


FIG. 3. (Color online) (a) NEXAFS TEY spectra around the carbon *K*-edge of a 30 nm thick LCP thin film. Spectra were recorded for *s* (red circles) and *p* polarization at $\theta = 20^\circ$ (blue diamonds). (b) Reflectivity R of an LCP film in *s* (red symbols) and *p* (blue symbols) polarization. Energy scans (sample D₂) at different incidence angles (horizontally offset for clarity) of $\theta = 5^\circ$ (top curves), 8° (middle curves), and 15° (bottom curves). The dashed line indicates the energy of 284.8 eV, where R vs grazing angle θ divided by the Fresnel reflectivity R_F of the silicon substrate is shown for sample D₁ (c).

lated numerically using the Euler-Maclaurin formula, taking every other data point to avoid singularities.²⁴ Off-resonant absorption data were interpolated from the CXRO database.²⁰ With an integration range between 10 eV and 30 keV and an equidistant step size of 0.1 eV, we were able to reproduce the off-resonant database values for f_1 in the relevant energy range and to obtain reliable values at the sharp NEXAFS resonances.

The absorption coefficient μ in *s* and *p* incidence can be calculated from Ref. 5

$$s \text{ pol} : \mu_s = \frac{3\mu_{\text{iso}}}{4} [1 + \xi], \quad (3a)$$

$$p \text{ pol} : \mu_p = \frac{3\mu_{\text{iso}}}{4} [1 + \xi + \cos \theta (1 - 3\xi)], \quad (3b)$$

with an isotropic average μ_{iso} and an asymmetry of $0 \leq \xi \leq 1/3$. Since the absorption resonances from the different functional groups overlap significantly, the full energy-dependent anisotropic refractive index ellipsoid cannot be calculated from

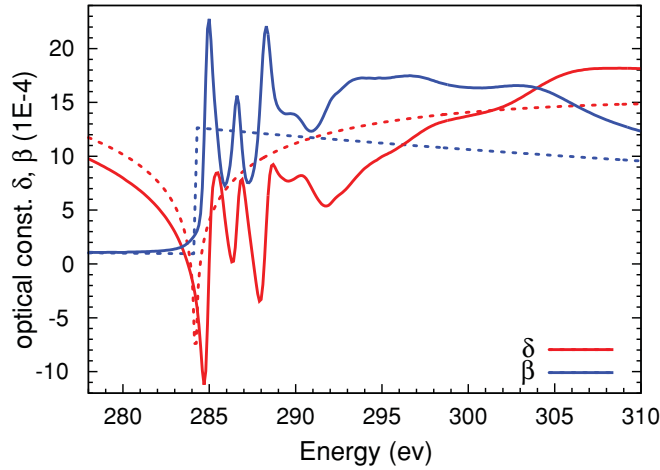


FIG. 4. (Color online) Isotropic averaged optical constants $n = 1 - \delta + I\beta$ of the LCP studied in this work. δ (blue curves) were calculated by Kramers-Kronig transformation [see Eq. (2)] from the NEXAFS spectroscopy data (solid curves) and from β for $C_{19}H_{15}O_5N$ given in the CXRO database (dashed curves).²⁰

the NEXAFS absorption data presented in this work in a straightforward way. For a more detailed discussion of this fundamental problem, see the work of Dressel *et al.*²⁵ and references therein. However, the components δ and β of the refractive index from this isotropic averaged μ_{iso} can then be calculated from Eq. (2) and are shown in Fig. 4 (solid lines) together with the reference values²⁰ for $C_{19}H_{15}O_5N$ (dotted lines) using a mass density of 1.2 g cm^{-3} .

B. Polarization-dependent resonant x-ray reflectivity

Off-resonant XRR data recorded at 250 eV exhibited no polarization dependence.¹⁵ Likewise, Fig. 3(b) shows that the reflectivity curves $R(E)$ at fixed angles below 282.5 eV and

above 287.0 eV are essentially polarization-independent. For x-ray reflectivity of isotropic systems, the relation $R_p = PR_s$, where $P = \cos^2 2\theta$ denotes the Lorentz polarization factor,²⁶ is not exactly fulfilled. However, it is a good approximation if the refractive index is close to unity, i.e., $\delta \ll 1$ and $\beta \ll 1$, leading to a Brewster angle θ_B close to 45° . Thus, differences between R_s and R_p are expected predominantly above absorption edges and at larger scattering angles. While NEXAFS spectroscopy provided no clear evidence for a preferred orientation of the ester groups at the free surface, there is significant interaction of the polar C=O bond with the hydrophilic OH-terminated SiO_2 substrate. While this would not affect the surface-sensitive NEXAFS TEY spectra, it might induce a preferred orientation adjacent to the buried interface, leading to an anisotropy in the resonant reflectivity signal around the ester resonance. These two mechanisms can explain the small intensity offset above 287.5 eV in the 8° and 15° curves.

The strong differences in the reflectivity recorded in s and p incidence that appear in the vicinity of the absorption resonance associated with the phenylene and nitrile π systems (see Fig. 5) are consistent with the NEXAFS data exhibiting strong dichroism from surface alignment of the functional groups in the LCP side chains. Fringes in $R(q)$ for s and p polarization are shifted with respect to each other in vertical momentum transfer [Fig. 3(c)]. To highlight the differences for different polarizations, the data in p incidence were normalized by P . Figure 6 shows the asymmetry $(R_p - PR_s)/(R_p + PR_s)$ for a selection of reflectivity data collected in s and p incidence. From this graph, we can clearly see that the degree and direction of these shifts, as well as the differences in the oscillation amplitudes, depend strongly on the energy of the incident x rays. With increasing scattering angle, the differences tend to decrease and finally vanish at normal incidence where the projections of the electric-field vectors on the surface plane become equal.

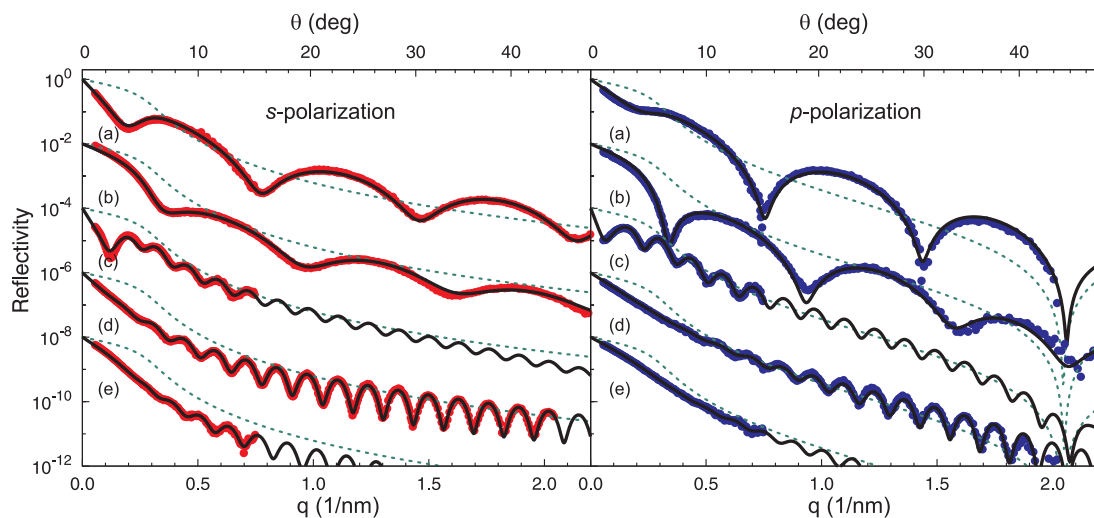


FIG. 5. (Color online) Experimental (circles) and calculated reflectivity patterns obtained by parameter refinement (solid black curves) in s (left) and p incidence (right) for different x-ray energies E and film thicknesses d . For details of sample B with 9.6 nm thickness measured at 284.8 eV (a), 285.4 eV (b), and sample D_1 with 49.0 nm at 284.4 eV (c), 284.8 eV (d), and 285.0 eV (e); see Table I. Each curve is vertically offset by a factor of 100. The Fresnel reflectivity of the substrate (silicon, dotted green curve) is added for reference. The incidence angle θ refers to an x-ray energy of 284.8 eV.

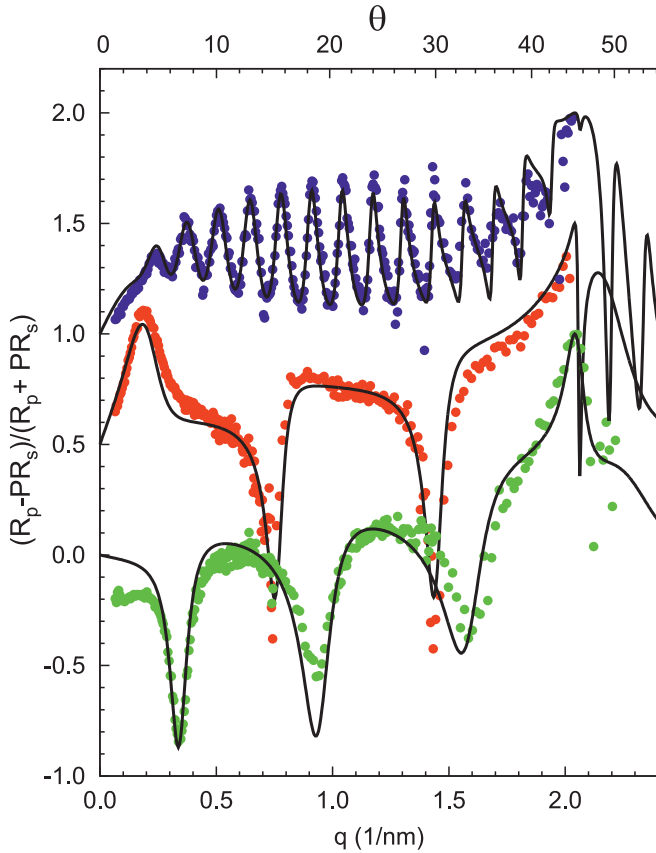


FIG. 6. (Color online) Asymmetry $(R_p - PR_s)/(R_p + PR_s)$ of the reflectivity data (symbols) and the calculated curves (lines) for sample B at 285.4 eV (bottom), 284.8 eV (middle), and D1 at 284.8 eV (top). Each curve is vertically offset by 0.5 for clarity.

At the phenylene and nitrile resonances, we found noticeable intensity for p incidence near the Brewster angle (Fig. 5), while off-resonance the reflectivity vanishes¹⁵ as expected for an isotropic system. However, anisotropic films with a parallel component of the optical axis with respect to the sample surface can be optically active.²⁷ This effect becomes particularly noticeable around the Brewster angle where in p incidence a system composed of isotropic materials reflects zero intensity, while at resonant energies partial reflectance was found in Fig. 5(b). Such an orientation with the long axis (see Fig. 1) in the surface plane is in line with the results from our NEXAFS data. Furthermore, planar anchoring with a vanishing perpendicular component was found in Ref. 16.

Cross-polarized light microscopy data on a similar nematic liquid crystalline polymer sample²⁸ showed domains with different in-plane orientations φ and a size of approximately 50 μm . The samples studied in our work are too thin to observe birefringence in the visible spectrum. Table II compiles the vertical d_v and horizontal d_h incident beam size and the footprint on the sample l_θ for different grazing angles θ . In all cases, the illuminated sample area was large compared to the domain size and we never observed rapid changes in the reflection pattern or the NEXAFS spectra that could be attributed to different domains when the samples were moved by distances comparable to the beam size. The transmission $T(d)$ of a film of thickness

d comprised of domains with different absorption coefficients $\mu(\varphi)$ cannot be calculated from the averaged value and vice versa,

$$T(d) = \frac{1}{2\pi} \int_{\varphi} d\varphi e^{-\mu(\varphi)d} \neq e^{-\frac{d}{2\pi} \int_{\varphi} d\varphi \mu(\varphi)}. \quad (4)$$

However, since the electron escape depth for TEY is small compared to the x-ray absorption length, the measured photocurrent is a good approximation of the averaged absorption coefficient. Likewise, the XRR pattern from a domain structure is generally not equal to the reflectivity from the spatially averaged profile. In particular, a film with an averaged refractive index and an optical axis parallel to the surface normal would not be optically active and thus is incompatible with our experimental findings. This justifies the assumption that the measured reflectivity signal is an incoherent average over several domains of different, random in-plane orientations φ . Thus, while the NEXAFS TEY spectra are not sensitive to the real crystallographic optical properties of the individual domains, XRR is.

C. Calculation of XRR curves and parameter refinement

For quantitative analysis of $R(q)$, we employed an algorithm based on Berreman's 4×4 matrix method¹³ for reflection and transmission in stratified media that serves as an extension of the Parratt formalism²⁹ for anisotropic systems. The x-ray reflectivity from a slab model including the silicon substrate, the native oxide, and a uniaxial layer with its optical axis laying parallel to the surface was calculated as described by Wöhler *et al.*²⁷ Interfacial width was treated by slicing the profile in 2 \AA thick layers.² To account for random in-plane orientation φ of the liquid crystalline domains, $R(q)$ for five nonsymmetry-related configurations was incoherently averaged. (A full description of the orientational distribution of the LCP side chains would require additional parameters. Here we assume that the side-chain orientation around the long axis is isotropic.) Optical properties for the substrate and off-resonant XRR data were calculated from tabulated values.² To take into account the large dynamic range of the observed reflectivity signal of up to seven orders of magnitude, the cost function Δ in the parameter refinement algorithm was calculated on a logarithmic scale,

$$\Delta = \sqrt{\langle \delta^2 \rangle - \langle \delta \rangle^2}, \quad (5a)$$

$$\alpha = e^{\langle \delta \rangle}, \quad (5b)$$

$$\delta_i = \ln \frac{R_i^{\text{cal}}}{\alpha I_i^{\text{exp}}}, \quad (5c)$$

with the global scaling parameter α for the incident x-ray flux. I_i^{exp} denotes the experimental data points, and R_i^{cal} the associated calculated reflectivity. An adaptive simulated annealing algorithm developed by Ingber³⁰ was employed for parameter refinement. Thicknesses, interfacial roughnesses, and mass densities of the LCP thin films were determined from off-resonant data sets and are compiled in Table I. For resonant XRR, the four independent components of the uniaxial complex refractive index ellipsoid of a single LCP domain were parametrized by the real f_1 and imaginary

f_2 part of the resonant molecular x-ray form factors for an x-ray beam with its electric field vector perpendicular and parallel to the optical axis. Self-consistent values were obtained by simultaneous fitting of experimental data in s and p incidence with the same parameter set for each x-ray energy and sample. Choices for parameter ranges and starting values were guided by the NEXAFS spectroscopy data and adjusted iteratively to obtain a converging set of final parameters.

The patterns obtained by parameter refinement of the XRR data using the Berreman formalism quantitatively reproduce all the observed shifts in the interference fringes, their modulation, as well as the overall decay of the reflectivity curves, as shown in Fig. 5. Likewise, the model reproduces all the features of the asymmetry curves (Fig. 6) that are most pronounced around the interference minima and close to the Brewster angle.

The real and imaginary parts of the molecular x-ray form factors perpendicular and parallel to the optical axis are compiled in Fig. 7. In particular, around the phenylene π^* resonance, the peak position and shape of f_2 as well as the characteristic dipolar shape of f_1 follow the energy dependence of the isotropic values calculated from NEXAFS spectra. This proves that the real and imaginary parts of the molecular x-ray form factors obtained by fitting the reflectivity data at different x-ray energies are generally Kramers-Kronig consistent, even though this constraint was not imposed in the data analysis. This results from their distinct contributions to the reflectivity signal, especially in the resonant range where both δ and β are large or change rapidly with energy.

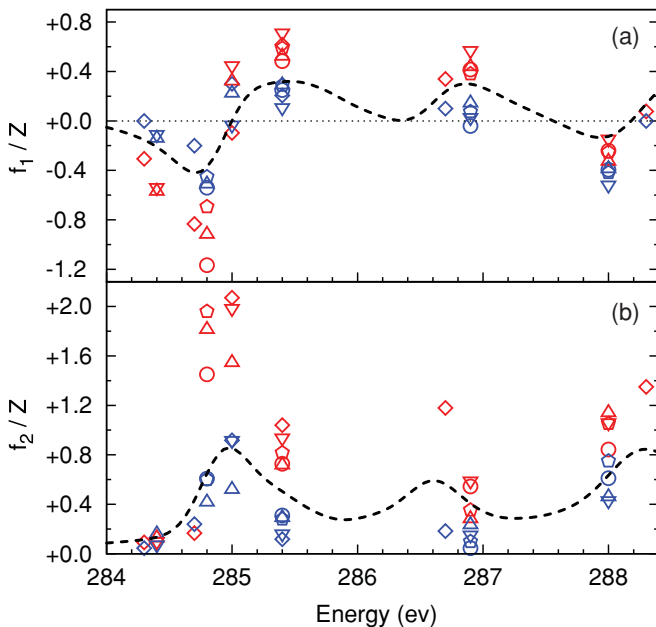


FIG. 7. (Color online) (a) Real f_1 and (b) imaginary part f_2 of the molecular x-ray form factors normalized by the number of electrons Z for a uniaxial LCP domain with the polarization perpendicular (red) and parallel (blue) to the optical axis. Values were obtained by parameter refinement of the XRR data from sample A (circles), B (pentagons), C (diamonds), D_1 (triangles up), D_2 (triangles down), and from NEXAFS TEY spectra (dashed black curves).

Differences of about a factor of 3 between the perpendicular and parallel f_2 components reflect the high orientational order of the phenylene groups within the liquid crystalline domains. This is consistent with the observation that the parameters of the refractive indices tend to be thickness-independent and the experimental data are reproduced perfectly by a homogeneous LCP slab, i.e., the orientation induced by the interfaces persists through the entire film.

Figures 5 and 6 indicate that the errors of the extracted parameters are not limited by the counting statistics of the experimental data but by factors such as a slight misalignment, sample inhomogeneity, and the assumptions in modeling and calculation of the reflectivity. An estimate of the combined error is given by the scatter of the parameters shown in Fig. 7 for a common energy obtained from independent reflectivity data sets that were measured at different beamlines and on different samples. Thus, while there is some noise evident in the resulting f_1 and f_2 values, their general Kramers-Kronig consistency is very robust and not affected by the systematic errors.

IV. CONCLUSIONS

Resonant soft XRR has the capabilities to study thin film structures of organic materials that exhibit only a low scattering contrast for hard x-rays.³¹ Here we extended this method, showing that molecular orientation in noncrystalline, anisotropic soft matter systems can be probed by resonant reflectivity in s and p incidence. The refractive index ellipsoid of the LCP domains was obtained by a quantitative analysis using the Berreman formalism. For isotropic materials and those with high symmetry, optical constants can be calculated directly from absorption spectra. However, low-symmetry systems with spectral features from different entities can impede a straightforward analysis.²⁵ Thus, the results from XRR can serve as a comparison and reference for *ab initio* calculations of the dielectric tensor. The precise depth-profiling capability of x-ray reflectivity with nanometer resolution and access to buried interfaces distinguishes XRR from NEXAFS spectroscopy and optical methods. While the LCP films studied here have depth-independent anisotropy, polarization-dependent XRR has the potential to study depth-dependent molecular orientation in a wide range of interesting and more disordered systems that cannot be obtained by any other established technique. Examples include conductive polymers for organic electronics and structural anisotropy in membrane materials for gas separation.

ACKNOWLEDGMENTS

This work was supported by the US Department of Energy's Office of Basic Energy Sciences through the Advanced Light Source, the Laboratory Directed Research and Development Program of Lawrence Berkeley Natl. Lab., and the Program "Fundamental Structural Studies of Hybrid Biomolecular Materials using Scattering Techniques" (M.V.) under Contract No. DE-AC02-05CH11231, and through the Center for Gas Separations Relevant to Clean Energy Technologies, an Energy Frontier Research Center (B.J.) under Award No. DE-SC0001015. A US-Spain Fulbright award supported M.V.

for part of this work. Data were acquired at the BEAR end station at ELETTRA Synchrotrone Trieste and at BL4.0.2 and BL6.3.2 at the ALS, Berkeley. We gratefully thank Elke Arenholz and Marco Liberati for their assistance in using BL4.0.2.

APPENDIX: SYNCHROTRON BEAMLINES FOR XRR

A. Mobile UHV scattering chamber at BL4.0.2, Advanced Light Source, Berkeley

Beamline 4.0.2 is optimized for magnetic spectroscopy³² and provides a high flux of nearly 10^{12} photons/s. It is equipped with an Apple-II Elliptical Polarizing undulator³³ for various x-ray polarizations including linear s and p and provides a free beam port that can accommodate mobile user instruments such as the UHV scattering chamber developed and operated by J. B. Kortright. For the experiments around the C K edge, the beamline was operated on the first undulator harmonic using a 700 1/mm grating and a monochromator entrance and exit slit width between 15 and 20 μm . At 285 eV, this results in a resolving power of approximately 7000 and a photon flux at the sample position of about 3×10^8 photons/s for s polarization and 1×10^8 photons/s for p (0.15 μm aluminum window, 0.6 μm silver filter).

B. Bending magnet for emission absorption and reflectivity (BEAR), ELETTRA, Synchrotrone Trieste

The BEAR instrument³⁴ is installed at the bending magnet BL8.1 L. It covers the spectrum from the visible to soft x rays (3 eV–1.6 keV), and is particularly suited for experiments in the energy range between the carbon and oxygen K edge. It is equipped with a reflectometer end station, working in linear and (variable) elliptically polarized light. A resolving power better than 2000 at 290 eV was obtained with the 1200 1/mm grating, high flux mode, 50 μm monochromator exit slit. Additional measurements on the degree of linear polarization using a tungsten-silicon multilayer confirmed a P_L (Ref. 35) better than 0.96 at 285 eV and 0.93 at 288.5 eV respectively.

C. Calibration and standards beamline of the Center for X-Ray Optics, BL6.3.2, Advanced Light Source, Berkeley

For sample characterization and comparison with the polarization-dependent data, x-ray reflectivity curves were measured at BL6.3.2.^{18,19} The beamline parameters were a 600 1/mm monochromator grating, a 35 μm exit slit width; a 3, 1, or 0.35 mm aperture to adjust incident flux for the different q ranges; a titanium filter; a nickel order sorter; and a Burle CEM detector.

*Present address: Max Planck Institute for Polymer Research, 55128 Mainz, Germany, meizer@mpip-mainz.mpg.de

†Present address: ALBA Synchrotron Light Source, 08290 Cerdanyola del Vall's, Barcelona, Spain.

¹J. Daillant, *Curr. Opin. Colloid Interface Sci.* **14**, 396 (2009).

²M. Tolan, *X-Ray Scattering from Soft Matter Thin Films* (Springer, Berlin, 1999).

³G. E. Mitchell, B. G. Landes, J. Lyons, B. J. Kern, M. J. Devon, I. Koprinarov, E. M. Gullikson, and J. B. Kortright, *Appl. Phys. Lett.* **89**, 044101 (2006).

⁴T. Araki, H. Ade, J. M. Stubbs, D. C. Sundberg, G. E. Mitchell, J. B. Kortright, and A. L. D. Kilcoyne, *Appl. Phys. Lett.* **89**, 124106 (2006).

⁵J. Stöhr, *NEXAFS Spectroscopy*, 2nd ed. (Springer, Santa Clara, 2003).

⁶C. Wang, T. Araki, and H. Ade, *Appl. Phys. Lett.* **87**, 214109 (2005).

⁷S. Swaraj, C. Wang, T. Araki, G. Mitchell, L. Liu, S. Gaynor, B. Deshmukh, H. Yan, C. R. McNeill, and H. Ade, *Eur. Phys. J.* **167**, 121 (2009).

⁸S. Roy *et al.*, *Phys. Rev. Lett.* **95**, 047201 (2005).

⁹A. Verna, B. A. Davidson, Y. Szeto, A. Y. Petrov, A. Mirone, A. Giglia, N. Mahne, and S. Nannarone, *J. Magn. Magn. Mater.* **322**, 1212 (2010).

¹⁰S. M. Valvidares, M. Huijben, P. Yu, R. Ramesh, and J. B. Kortright, *Phys. Rev. B* **82**, 235410 (2010).

¹¹H.-C. Mertins, P. M. Oppeneer, S. Valencia, W. Gudat, F. Senf, and P. R. Bressler, *Phys. Rev. B* **70**, 235106 (2004).

¹²H. Ade and A. P. Hitchcock, *Polymer* **49**, 643 (2008).

¹³D. W. Berreman, *J. Opt. Soc. Am.* **62**, 502 (1972).

¹⁴J. F. Mano and J. J. M. Ramos, *Thermochim. Acta* **323**, 65 (1998).

¹⁵See supplemental material at [<http://link.aps.org/supplemental/10.1103/PhysRevB.83.155406>] for details.

¹⁶B. Jerome, J. Commandeur, and W. H. D. Jeu, *Liq. Cryst.* **22**, 685 (1997).

¹⁷A. M. Donald, A. H. Windle, and H. Hanna, *Liquid Crystalline Polymers* (Cambridge University Press, Cambridge, 2006).

¹⁸J. H. Underwood, E. M. Gullikson, M. Koike, P. J. Batson, P. E. Denham, K. D. Franck, R. E. Tackaberry, and W. F. Steele, *Rev. Sci. Instrum.* **67**, 1 (1996).

¹⁹J. H. Underwood and E. M. Gullikson, *J. Electron Spectrosc.* **92**, 265 (1998).

²⁰B. L. Henke, E. M. Gullikson, and J. C. Davis, *At. Data Nucl. Data Tables* **54**, 181 (1993).

²¹O. Dhez, H. Ade, and S. G. Urquhart, *J. Electron Spectrosc. Relat. Phenom.* **128**, 85 (2003).

²²R. D. L. Kronig, *J. Opt. Soc. Am.* **12**, 547 (1926).

²³C. T. Chantler, *J. Phys. Chem. Ref. Data* **29**, 597 (2000).

²⁴K. Ohta and H. Ishida, *Appl. Spectrosc.* **42**, 952 (1988).

²⁵M. Dressel, B. Gompf, D. Faltermeier, A. K. Tripathi, J. Pflaum, and M. Schubert, *Opt. Express* **16**, 19770 (2008).

²⁶P. Kirkpatrick, *Phys. Rev.* **29**, 632 (1927).

²⁷H. Wöhler, M. Fritsch, G. Haas, and D. A. Mlynski, *J. Opt. Soc. Am. A* **8**, 536 (1991).

²⁸T. W. Clyne, DoITPoMS Micrograph Library, Record 612, Univ. Cambridge (2002).

²⁹L. G. Parratt, *Phys. Rev.* **95**, 359 (1954).

- ³⁰L. Ingber, *Math. Comput. Model.* **18**, 29 (1993).
- ³¹C. Wang, A. Garcia, H. Yan, K. E. Sohn, A. Hexemer, T. Q. Nguyen, G. C. Bazan, E. J. Kramer, and H. Ade, *J. Am. Chem. Soc.* **131**, 12538 (2009).
- ³²A. T. Young *et al.*, *Nucl. Instrum. Methods Phys. Res. A* **467/468**, 549 (2001).
- ³³A. T. Young, E. Arenholz, S. Marks, R. Schlueter, C. Steier, H. A. Padmore, A. P. Hitchcock, and D. G. Castner, *J. Synchrotron Rad.* **9**, 270 (2002).
- ³⁴S. Nannarone *et al.*, *Synchrotron Radiation Instrumentation: Eighth International Conference*, AIP Conf. Proc. No. 705 (AIP, New York, 2004), p. 450.
- ³⁵J. B. Kortright *et al.*, *Rev. Sci. Instrum.* **67**, 3363 (1996).